



Measurement of Z boson production cross-section in pp collisions at $\sqrt{s} = 5.02$ TeV

LHCb collaboration[†]

Abstract

The first measurement of the Z boson production cross-section at centre-of-mass energy $\sqrt{s} = 5.02$ TeV in the forward region is reported, using pp collision data collected by the LHCb experiment in year 2017, corresponding to an integrated luminosity of $100 \pm 2 \text{ pb}^{-1}$. The production cross-section is measured for final-state muons in the pseudorapidity range $2.0 < \eta < 4.5$ with transverse momentum $p_T > 20 \text{ GeV}/c$. The integrated cross-section is determined to be

$$\sigma_{Z \rightarrow \mu^+ \mu^-} = 39.6 \pm 0.7 (\text{stat}) \pm 0.6 (\text{syst}) \pm 0.8 (\text{lumi}) \text{ pb}$$

for the di-muon invariant mass in the range $60 < M_{\mu\mu} < 120 \text{ GeV}/c^2$. This result and the differential cross-section results are in good agreement with theoretical predictions at next-to-next-to-leading order in the strong coupling.

Based on a previous LHCb measurement of the Z boson production cross-section in $p\text{Pb}$ collisions at $\sqrt{s_{NN}} = 5.02$ TeV, the nuclear modification factor $R_{p\text{Pb}}$ is measured for the first time at this energy. The measured values are $1.2^{+0.5}_{-0.3} (\text{stat}) \pm 0.1 (\text{syst})$ in the forward region ($1.53 < y_\mu^* < 4.03$) and $3.6^{+1.6}_{-0.9} (\text{stat}) \pm 0.2 (\text{syst})$ in the backward region ($-4.97 < y_\mu^* < -2.47$), where y_μ^* represents the muon rapidity in the centre-of-mass frame.

Submitted to JHEP

© 2023 CERN for the benefit of the LHCb collaboration. CC BY 4.0 licence.

[†]Authors are listed at the end of this paper.

1 Introduction

Measurements of the $pp \rightarrow Z \rightarrow \mu^+\mu^-$ process¹ provide important tests of the quantum chromodynamics (QCD) and electroweak (EW) sectors of the Standard Model. High precision measurements of the Z boson production cross-section at various experiments provide valuable insights for testing theoretical predictions [1–9], which are further validated through their comparison with precision perturbative QCD calculations up to the order of α_s^3 [8, 9].

High precision measurements of the Z boson production cross-sections at different rapidities at LHCb provide important constraints on parton distribution functions (PDFs). Results from deep inelastic scattering and hadronic collisions [10–25], parameterized in terms of the Bjorken variable, x , indicating the fraction of the proton momentum carried by a single parton, are used in the global fits of the PDFs. However, these measurements provide limited information on the PDFs in the very large ($x \sim 0.8$) or very small ($x \sim 10^{-4}$) Bjorken- x regions. This leads to large uncertainties on the PDFs, and on the theoretical predictions that make use of them. Forward acceptance of the LHCb detector covers a unique region of phase space, allowing the measurement of highly boosted Z boson candidates. Measurements within this region are sensitive to both large and small Bjorken- x values. Previous measurements of single W and Z production by the LHCb collaboration [26–32] have been included in PDF calculations [33–41]; the LHCb data contribute significantly to the precision of these determinations of the quark PDFs at large and small values of x .

In addition, the Z boson production cross-section is useful for constraining nuclear PDFs (nPDFs), providing a clean probe of nuclear-matter effects in the initial state. These effects are typically studied in terms of the nuclear modification factor, $R_{p\text{Pb}}$, defined as the ratio of the yield observed in $p\text{Pb}$ collisions to that in pp collisions, scaled by the mean number of nucleon-nucleon interactions. This quantity is used to study the modification of particle production in heavy-ion collisions compared to pp collisions. The LHCb experiment published the first inclusive Z production result in $p\text{Pb}$ collisions at a nucleon-nucleon centre-of-mass energy of $\sqrt{s_{NN}} = 5.02 \text{ TeV}$ [42]. However, the nuclear modification factors are not reported for this collision energy due to the absence of a measurement for the cross-section in pp collisions. With this new measurement for the Z boson production cross-section in pp collisions at $\sqrt{s} = 5.02 \text{ TeV}$, the nuclear modification factors in the forward region and backward regions are been reported for the first time. The forward and backward regions, defined by the muon rapidity y_μ^* in the centre-of-mass frame, are $1.53 < y_\mu^* < 4.03$ and $-4.97 < y_\mu^* < -2.47$, as the $p\text{Pb}$ collision system experiences an asymmetric distribution of beam energy.

In this article, the integrated and differential Z boson production cross-sections are measured at the Born level in QED, using pp collision data collected by the LHCb detector at a centre-of-mass energy of $\sqrt{s} = 5.02 \text{ TeV}$ in 2017, corresponding to an integrated luminosity of 100 pb^{-1} [43]. The production cross-sections are measured in a fiducial region that closely matches the acceptance of the LHCb detector, following the analysis strategy developed in Ref. [32]. The fiducial region is defined by requiring that both muons have a pseudorapidity in the range of $2.0 < \eta < 4.5$ and transverse momentum

¹The production process should be interpreted as $pp \rightarrow Z/\gamma^* \rightarrow \mu^+\mu^-$ in the strict sense. In this article, the label Z boson is defined to also include contributions from virtual photons and the interference between the Z boson and the virtual photon.

$p_T > 20 \text{ GeV}/c$, and that the di-muon invariant mass is the interval $60 < M_{\mu\mu} < 120 \text{ GeV}/c^2$. The differential cross-section is measured as a function of the Z boson rapidity (y^Z), transverse momentum (p_T^Z) and ϕ_η^* [44], which is defined as

$$\phi_\eta^* = \tan [(\pi - \Delta\phi^{\ell\ell})/2] \sin(\theta_\eta^*), \quad (1)$$

where $\Delta\phi^{\ell\ell}$ represents the difference in the azimuthal angle between the two muons in the laboratory frame. The variable θ_η^* is defined by $\cos(\theta_\eta^*) = \tanh[(\eta^- - \eta^+)/2]$, with η^- and η^+ denoting the pseudorapidities of the negatively and positively charged muons in the laboratory frame. The observable ϕ_η^* probes similar physics as the transverse momentum p_T^Z , but is measured with near-perfect resolution.

2 Detector and simulation

The LHCb detector [45, 46] is a single-arm forward spectrometer covering the pseudorapidity range $2 < \eta < 5$, designed for the study of hadrons containing b or c quarks. The detector includes a high-precision tracking system consisting of a silicon-strip vertex detector surrounding the pp interaction region [47], a large-area silicon-strip detector (TT) [48], located upstream of a dipole magnet with a bending power of about 4 Tm, and three stations of silicon-strip detectors and straw drift tubes [49] placed downstream of the magnet. The tracking system provides a measurement of the momentum, p , of charged particles with a relative uncertainty that varies from 0.5 % at low momentum to 1.0 % at 200 GeV/ c . The minimum distance of a track to a primary pp collision vertex, the impact parameter, is measured with a resolution of $(15 + 29/p_T) \mu\text{m}$, where p_T is the component of the momentum transverse to the beam, in GeV/ c . Photons, electrons and hadrons are identified by a calorimeter system consisting of scintillating-pad and preshower detectors, an electromagnetic and a hadronic calorimeter. Muons are identified by a system composed of alternating layers of iron and multiwire proportional chambers [50]. The online event selection is performed by a trigger [51], which consists of a hardware stage, based on information from the calorimeter and muon systems, followed by a software stage, which applies a full event reconstruction.

Simulation is used to model the effects of the detector acceptance and the imposed selection requirements. In the simulation, pp collisions are generated using PYTHIA [52, 53] with a specific LHCb configuration [54]. Final state radiation (FSR) is generated using PHOTOS [55]. The interaction of the generated particles with the detector, and its response, are implemented using the GEANT4 toolkit [56] as described in Ref. [57].

3 Event selection and background estimation

The muon triggers are responsible for the online event selection. At the hardware trigger stage, a muon candidate with high p_T is required. The muon candidate is required to have $p_T > 6 \text{ GeV}/c$ and $p > 8 \text{ GeV}/c$, along with a good track fit quality in the first software trigger stage. In the second software trigger stage, an additional requirement of $p_T > 12.5 \text{ GeV}/c$ is imposed on the muon candidate. For a $Z \rightarrow \mu^+\mu^-$ candidate, it is necessary for at least one of the muons to pass both the hardware and software trigger stages. These stages ensure the identification of the particle as a muon with high transverse momentum.

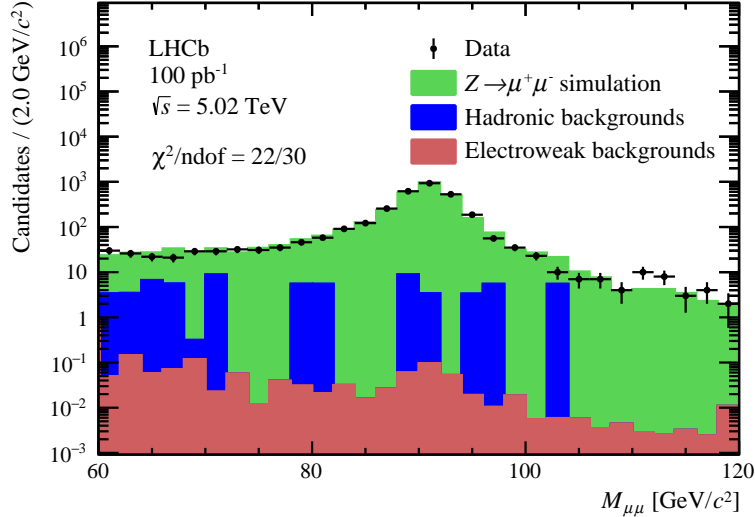


Figure 1: Mass distribution of the $Z \rightarrow \mu^+\mu^-$ signal candidates. The data are overlaid with model of the signal and background models. The signal component is scaled such that the sum of the signal and background matches the integral of the data.

A high purity $Z \rightarrow \mu^+\mu^-$ sample is reconstructed from a pair of opposite-signed tracks identified as muons. The invariant mass of the di-muon is required to be within the range $60 < M_{\mu\mu} < 120 \text{ GeV}/c^2$. For each muon track, the fiducial requirements are $p_T > 20 \text{ GeV}/c$ and pseudorapidity in the range $2.0 < \eta < 4.5$. The muons are required to have momentum measurements with relative uncertainties below 10%. In total, 3265 $Z \rightarrow \mu^+\mu^-$ candidates meet these selection criteria, and the distribution of the di-muon invariant mass for the selected candidates is shown in Fig. 1.

The background contribution from decays of heavy flavour hadrons is estimated using two control samples. Tracks from heavy flavour decays degrade the primary vertex (PV) fit quality when included in the PV fit, since the heavy hadron travels a certain distance before decaying. Hence, the first control sample is obtained by applying a requirement that the selected candidate have a PV with a low fit quality ($\chi^2 > 95$). Additionally, muons produced from semileptonic decays of heavy flavour hadrons are less isolated. The variable I_μ is defined as the ratio of the muon p_T to the vector sum of the p_T of all charged particles in a cone around the muon, where the cone is constrained using the radius parameter $R = \sqrt{\Delta\eta^2 + \Delta\phi^2} < 0.5$. The second control sample is selected by requiring that the two muons are not spatially isolated ($I_\mu < 0.91$) from other rest of the event.

The yields of these two control samples are determined from a fit to the di-muon invariant mass distributions, using an exponential function. The heavy flavour background is concentrated at low mass ($50 < M_{\mu\mu} < 70 \text{ GeV}/c^2$), so to obtain a larger sample and a more stable fit, the background yield is determined in the region $50 < M_{\mu\mu} < 110 \text{ GeV}/c^2$. The extrapolation corrects for the efficiency of the vertex quality and isolation requirements. The efficiency of the muon isolation (vertex quality) selection is calculated separately by applying the muon isolation requirement (vertex quality requirement) to the first (second) control sample. The estimated background contributions for these two subsamples are consistent, and the average value is taken as the background contribution from the heavy

flavour decay process, which is determined to be $(1.98 \pm 1.56)\%$ for the selected $Z \rightarrow \mu^+ \mu^-$ sample.

The contribution from the combinatorial background including misidentified hadrons and B - \bar{B} mixing is estimated using pairs of same-sign muons in the data. In the same-sign events, a muon from heavy flavour decay combined with a misidentified hadron are expected to make sizable contributions. After removing the contribution from heavy flavour processes, the contribution from misidentified hadrons is determined to be negligible. The electroweak background contributions from the $t\bar{t}$, W^+W^- , $W^\pm Z$, ZZ and $Z \rightarrow \tau^+ \tau^-$ processes are estimated from the simulation, with leading-order (LO) to next-to-next-to-leading-order (NNLO) correction factors determined with the MCFM [58] package.

In summary, the total background contribution to the $Z \rightarrow \mu^+ \mu^-$ sample in the mass range $60 < M_{\mu\mu} < 120 \text{ GeV}/c^2$ is determined to be $(2.02 \pm 1.56)\%$ and the background composition of the candidate sample is summarised in Table 1. The data-driven backgrounds refer to processes involving heavy flavor decays and hadron misidentification, which are estimated based on the observed events in the data.

Table 1: Summary of the background composition in the $Z \rightarrow \mu^+ \mu^-$ data sample of candidates satisfying the signal selection.

Background	Estimation	Events	Fraction
Heavy flavour ($b\bar{b}$, $c\bar{c}$)	data-driven	65 ± 51	2.0×10^{-2}
Hadron misidentification	data-driven	0.20 ± 0.10	6.0×10^{-5}
$Z \rightarrow \tau^+ \tau^-$	Simulation	0.39 ± 0.12	1.2×10^{-4}
WZ/ZZ	Simulation	0.25 ± 0.04	7.7×10^{-5}
WW	Simulation	0.19 ± 0.02	5.8×10^{-5}
$t\bar{t}$	Simulation	0.14 ± 0.10	4.4×10^{-5}
Total		66 ± 51	2.0×10^{-2}

4 Cross-section determination

Only single-differential cross-section measurements are performed due to the limited sample yields. The differential production cross-section is measured as a function of y^Z , p_T^Z and ϕ_η^* , and the integrated cross-section is obtained by integrating over all bins, which are chosen based on the detector resolution and sample size. Indicating with a generic variable a , the differential cross-section is defined as

$$\frac{d\sigma_{Z \rightarrow \mu^+ \mu^-}}{da}(i) = \frac{N_Z(i) \cdot f_{FSR}^Z(i)}{\mathcal{L} \cdot \varepsilon^Z(i) \cdot \Delta a(i)}, \quad (2)$$

where the generic variable a represents the observable y^Z , p_T^Z or ϕ_η^* , the index i indicates the bin of the variable under study, $N_Z(i)$ is the signal yield in bin i after background subtraction, $f_{FSR}^Z(i)$ is the FSR correction factor (as discussed in Sec. 4.3), \mathcal{L} is the integrated luminosity, $\Delta a(i)$ is bin width for i -th bin (as presented in Tables 4 to 6 in Appendix B), and $\varepsilon^Z(i)$ is the total efficiency in the i -th bin.

To account for detector misalignment effects, the Z mass peak position and resolution in simulated events are corrected to be compatible with the data, using momentum scaling

and smearing factors [59]. The impact from this correction on the integrated cross-section measurement is found to be negligible.

4.1 Efficiency

The selection efficiencies are determined for the muon tracking, muon identification and trigger requirements. These are derived using the $Z \rightarrow \mu^+ \mu^-$ data and a tag-and-probe method [60].

In the determination of the tracking efficiency, a particle reconstructed in all the tracking subdetectors, and fulfilling the muon trigger and muon identification requirements, is used as the tag. An object reconstructed by combining hits in the muon stations and the TT downstream tracking stations, denoted as a MuonTT track, then acts as the probe. As described in Ref. [60], the tracking efficiency is calculated as the fraction of probe candidates matched with a reconstructed track. However, the precision of the measured tracking efficiency is limited by the low number of Z -boson candidates in the data sample. In this analysis, we therefore use the tracking efficiency $\varepsilon_{\text{Tracking}}^{\text{MC},5.02}$ found from the 5.02 TeV $Z \rightarrow \mu^+ \mu^-$ simulation, and apply a correction to this using a scale factor determined using the tag-and-probe method in the 13 TeV analysis [32], as

$$\varepsilon_{\text{Tracking}}^{\text{Data},5.02} = \varepsilon_{\text{Tracking}}^{\text{MC},5.02} \times \frac{\varepsilon_{\text{Tracking}}^{\text{Data},13}}{\varepsilon_{\text{Tracking}}^{\text{MC},13}}. \quad (3)$$

For the muon identification efficiency determination, the yield in the data sample is also limited which leads to statistical fluctuations in the results. Similar to the correction method employed for muon tracking efficiency, with the data and simulated ID efficiency already available from the published results at 13 TeV [32], a scale factor is applied to the 5.02 TeV simulation efficiency.

The efficiency of the muon trigger is determined with the tag-and-probe method, where a tag particle is chosen from a particle reconstructed in all tracking subdetectors, which must be identified and triggered as a muon. Meanwhile, the probe particle must pass all selection requirements used in the analysis apart from the trigger requirements. The invariant mass of tag and probe particles is further required to be within the range $[60,120] \text{ GeV}/c^2$, and the azimuthal separation, $|\Delta\phi|$, greater than 2.7 radians. The efficiency is computed as the ratio of the number of probes within the selected sample meeting the muon trigger criteria to the total number of probes.

After correcting the muon tracking efficiency using Eq. 3 and applying this correction method to the muon identification efficiency in a similar way, the determined muon tracking reconstruction efficiency $\varepsilon_{\text{Track}}^{\mu^\pm}$, identification efficiency $\varepsilon_{\text{ID}}^{\mu^\pm}$ and trigger efficiency $\varepsilon_{\text{Trig}}^{\mu^\pm}$ vary between 94% and 98%, 90% and 97%, 62% and 85% respectively. These determined efficiencies as a function of muon pseudorapidity are summarized in Appendix A.

This measurement follows the efficiency correction method employed in the 13 TeV analysis [32], which involved a one-dimensional efficiency correction based solely on the muon pseudorapidity. The validity of this correction method is ensured by conducting the so-called closure tests using simulated samples. The differences between this correction method and the true information from the simulation is considered as a source of systematic uncertainty (as discussed in Sec. 5).

With the previous muon efficiencies $\varepsilon_{\text{Track}}^{\mu^\pm}$, $\varepsilon_{\text{ID}}^{\mu^\pm}$, and $\varepsilon_{\text{Trig}}^{\mu^\pm}$ determined, the total efficiency ε^Z depends on the pseudorapidities of the two final-state muons and can be calculated as

$$\varepsilon^Z = \left(\varepsilon_{\text{Track}}^{\mu^+} \cdot \varepsilon_{\text{Track}}^{\mu^-} \right) \cdot \left(\varepsilon_{\text{ID}}^{\mu^+} \cdot \varepsilon_{\text{ID}}^{\mu^-} \right) \cdot \left(\varepsilon_{\text{Trig}}^{\mu^+} + \varepsilon_{\text{Trig}}^{\mu^-} - \varepsilon_{\text{Trig}}^{\mu^+} \cdot \varepsilon_{\text{Trig}}^{\mu^-} \right). \quad (4)$$

4.2 Unfolding

The detector resolution causes migration between kinematic bins. Due to the good angular resolution of the LHCb detector, negligible migration effects are observed among y^Z and ϕ_η^* bins.

To assess the necessity of using an unfolding method to correct the p_T^Z measurement at the reconstruction level, the ratio of the p_T^Z distribution before and after unfolding is calculated from data, and then compared to the ratio of the reconstructed p_T^Z distribution and the generated p_T^Z distribution, obtained from the simulated sample. Since notable migration is observed, the unfolding procedure is performed for the p_T^Z distribution, using the Bayesian unfolding method [61, 62].

4.3 Final state radiation correction

The measured cross-section is corrected to the Born level in QED, so that it can be directly compared with theoretical predictions. The final-state radiation (FSR) correction is developed and applied to the measurements, by comparing the RESBos [63] predictions with and without the implementation of PHOTOS [55], which corrects the quantities of muons after final state radiation to the Born level. The FSR corrections in bins of y^Z , p_T^Z and ϕ_η^* are shown in Fig. 2. The corrections for single-differential cross-section measurements are also presented in Appendix B.

5 Systematic uncertainties

To account for potential sources of systematic uncertainties in the cross-section measurements, several sources are considered. These uncertainties include the background estimation, the calibration of the momentum scale, the efficiency determination, the unfolding procedure, the results of efficiency closure tests, the FSR correction, and the measurement of the integrated luminosity.

The determination of the heavy flavour background uses the averaged yield between two methods as the background contribution. The associated uncertainty is calculated as the discrepancy between the background yields obtained from the two control samples. Additionally, a systematic uncertainty is introduced by varying the mass region and selection requirements of the control samples. The hadron misidentification and other backgrounds are estimated from the data and simulation, with the statistical uncertainties being treated as systematic uncertainties that depend on the limited size of the same-sign data and simulation samples. The systematic uncertainties on the $t\bar{t}$, W^+W^- , $W^\pm Z$, ZZ , and $Z \rightarrow \tau^+\tau^-$ components derive from the statistical uncertainties and theoretical uncertainties on the LO to NNLO correction factors. To estimate the uncertainty due to inadequate calibration of the detector, the momentum scaling and smearing correction for the simulation are studied in order to improve the modeling of the $Z \rightarrow \mu^+\mu^-$ data. Only a

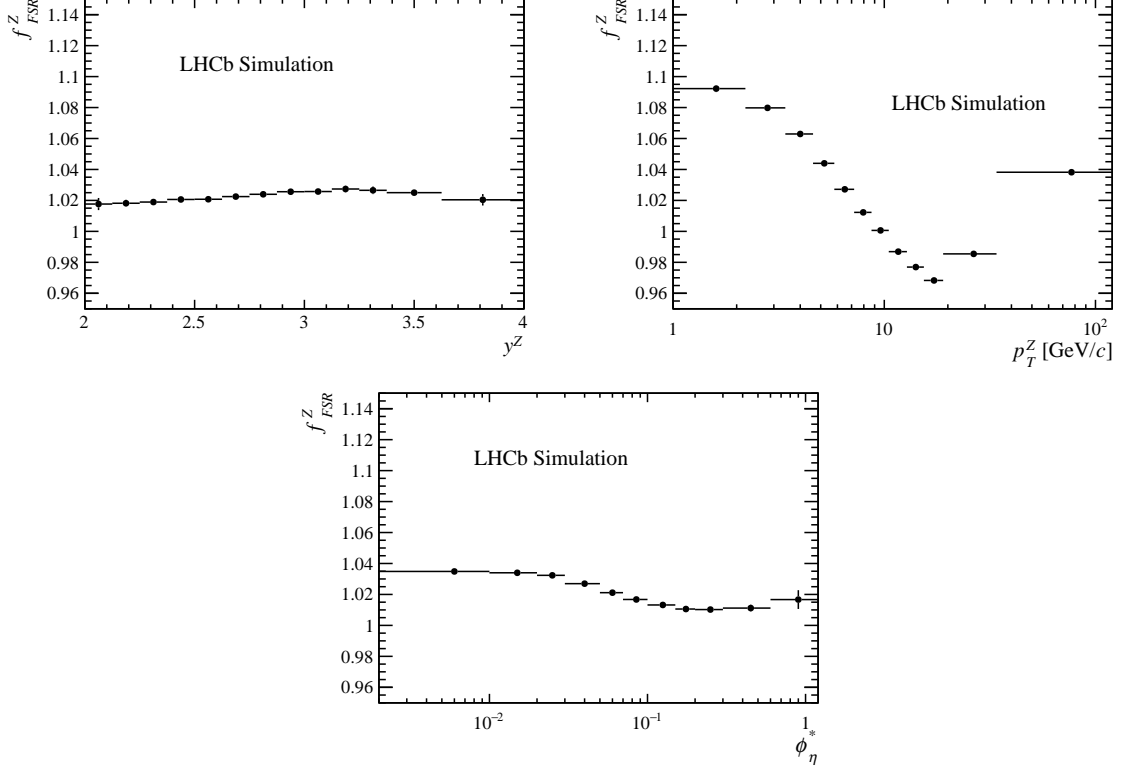


Figure 2: Final state radiation correction estimated for the (top-left) y^Z , (top-right) p_T^Z , and (bottom) ϕ_η^* differential cross-section measurements. The error bars represent the total (statistical and systematic) uncertainties.

small fraction, less than 0.01% of events, exhibits changes when comparing the simulation before and after studying the momentum scaling and smearing. This value is conservatively assigned as the systematic uncertainty related to the detector alignment. The impact from momentum calibration uncertainty on the integrated cross-section measurement is found to be negligible. However, the alignment uncertainty is considered and added for the p_T^Z distribution.

The track reconstruction and identification efficiencies for high p_T muons are calculated using simulation and data taking at $\sqrt{s} = 13$ TeV. The systematic uncertainties are determined by the size of the 5.02 TeV simulation samples and the uncertainties are propagated from the 13 TeV results. For the trigger efficiency, which is directly measured using control samples in the 5.02 TeV data, a systematic uncertainty is assigned for variations due to the limited size of the samples studied. As studied in Ref. [32], an additional systematic uncertainty is evaluated, based on the method used to determine the tracking efficiency. This is evaluated to be 0.47% which is already considered in the systematic uncertainty of the muon tracking efficiency.

To examine whether it is sufficient to perform efficiency corrections only as a function of the muon pseudorapidity variable or if the efficiency also depends on other variables such as muon p_T , a closure test is performed. The reconstructed event yields in simulation are adjusted using the efficiencies determined solely based on the muon pseudorapidity obtained from the simulation samples and then compared with the generated yield. The

Table 2: The uncertainties for the integrated $Z \rightarrow \mu^+ \mu^-$ cross-section measurement.

Source	$\Delta\sigma$ [pb]	$\Delta\sigma/\sigma$ [%]
Luminosity	0.79	2.00
Statistical	0.70	1.77
Tracking	0.40	1.01
Efficiency Closure	0.24	0.61
Trigger	0.21	0.54
Background	0.19	0.48
Identification	0.10	0.25
FSR	0.07	0.18
Calibration	$< 4.0 \times 10^{-3}$	< 0.01
Total Systematic (excl. lumi.)	0.56	1.42

differences, which do not exhibit any systematic pattern across the differential cross-section measurement regions, are attributed as an additional source of uncertainty.

To estimate the uncertainty attributed to the unfolding process, the p_T^Z distribution is unfolded using the so-called *Invert Approach* [64], which employs a simple inversion of the response matrix without regularisation. The deviation of the results from the *Bayesian Approach* [61, 62] is taken as a systematic uncertainty on the p_T^Z differential cross-section. The systematic uncertainty arising from the FSR correction is evaluated by comparing the default correction with one determined using the POWHEG generator showered using PYTHIA. The differences in FSR corrections between RESBOS with PHOTOS and POWHEG with PYTHIA are then taken into consideration as a systematic uncertainty. Regarding the data sample used, the luminosity is determined with a precision of 2.0% [43], which is quoted separately to the other sources of systematic uncertainty. The statistical and systematic uncertainties in the integrated cross-section measurement are listed in Table 2. The different sources of systematic uncertainty for each bin of the differential cross-sections are summarised in Tables 13 to 15 in Appendix D.

6 Results

6.1 Differential cross-section results

The single differential cross-sections in regions of y^Z , p_T^Z and ϕ_η^* are shown in Fig. 3, together with the ratios of theoretical predictions to data. The numerical results of single differential cross-section within each bin are summarised in Tables 16–18 in Appendix E.

The RESBOS [63] program performs resummation of large logarithms, up to next-to-next-leading-logarithm accuracy, within the Collins-Soper-Sterman resummation formalism [65–67] and matches to next-to-leading-order (NLO) fixed order calculations. The enhanced QCD prediction is obtained from the simulated $Z \rightarrow \mu^+ \mu^-$ sample, generated with RESBOS [63] using the CT18 PDFs [36] for all measurements. POWHEG-BOX [68–71] is an NLO generator, and can be interfaced with PYTHIA for QCD and EW showering. Although PYTHIA is a LO generator, it approximates higher order effects in initial and final states via a parton showering algorithm [72]. In this analysis, POWHEG-BOX is

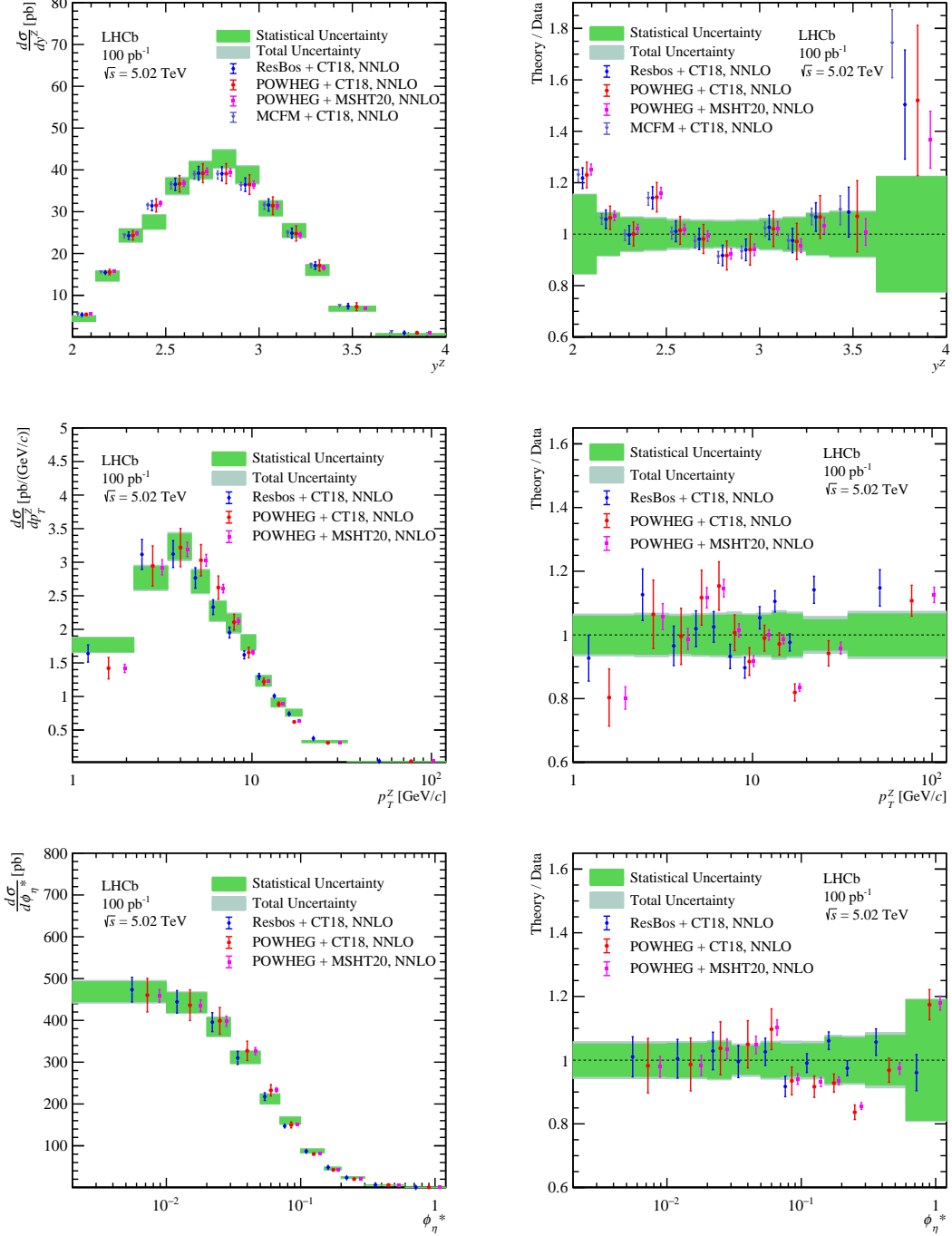


Figure 3: (Left) Measured single differential cross-section as a function of y^Z , p_T^Z and ϕ_{η}^* compared with different theoretical predictions. (Right) Ratio of theoretical predictions to measured values, with the horizontal bars showing the uncertainty from the PDFs. The green band, centered at unity, shows the uncertainty of the measurement.

used to generate $Z \rightarrow \mu^+ \mu^-$ events, followed by hadronization using PYTHIA for all measurements. The MCFM package [58], a fixed-order NNLO generator, is used here to estimate the Z boson production cross-section as a function of y^Z in the acceptance of

the LHCb detector.

For these three generators, different PDF sets NNPDF3.1 [37], NNPDF4.0 [38], MSHT20 [39], and CT18 [36] are employed to provide theoretical predictions. Measurements are in reasonable agreement with the different theoretical predictions. In both the lower and higher p_T^Z and ϕ_η^* region, the measurements agree with predictions from both RESBOS and POWHEG. For the measurement of y^Z , the theoretical predictions from the three generators are also compatible with the experimental results within the uncertainty range.

6.2 Correlation matrices

The event migration between bins causes statistical correlations, which are determined using simulation. Large correlations are found in the low- p_T^Z region and small correlations in the high- p_T^Z region, while the statistical correlations are negligible for both the y^Z and ϕ_η^* distributions.

For the differential cross-section measurements, background, alignment, efficiency closure test, and FSR uncertainties are assumed to be 50% correlated between different bins, while the luminosity uncertainty is considered to be 100% correlated. The calculated correlation matrices for the efficiencies are presented in Appendix C. Large correlations between different bins are present in the p_T^Z differential cross-section measurement, but small correlations are also present between most bins for the y^Z and ϕ_η^* measurements.

6.3 Integrated cross-section results

Using the LHCb 2017 pp collision data at $\sqrt{s} = 5.02$ TeV, the integrated Born-level Z boson production cross-section, with two muons in the final state and within the LHCb acceptance is

$$\sigma_{Z \rightarrow \mu^+ \mu^-} = 39.6 \pm 0.7 \text{ (stat)} \pm 0.6 \text{ (syst)} \pm 0.8 \text{ (lumi)} \text{ pb} \quad (5)$$

where the uncertainties are due to statistical effects, systematic effects, and the luminosity measurement, respectively.

In this article, the Z boson is defined to also include contributions from virtual photons, and the interference between them since they cannot be distinguished experimentally. The measured results obtained for the total cross-section of the $pp \rightarrow Z \rightarrow \mu^+ \mu^-$ process at 5.02 TeV in the fiducial region of the LHCb detector have been compared to the predictions obtained using MCFM with CT18NNLO and other theoretical models, including POWHEG-Box with NNPDF3.1, NNPDF4.0, MSHT20, CT18, and RESBOS with CT18, all of which account for both statistical and PDF uncertainties. These theoretical predictions are compared to the results in Fig. 4, which demonstrate a reasonable agreement.

By comparing the theoretical predictions at different center-of-mass energies provided by MCFM, with the experimental measurements previously obtained by LHCb at $\sqrt{s} = 7, 8$ and 13 TeV, as illustrated in Fig. 5, a good level of consistency can be observed overall.

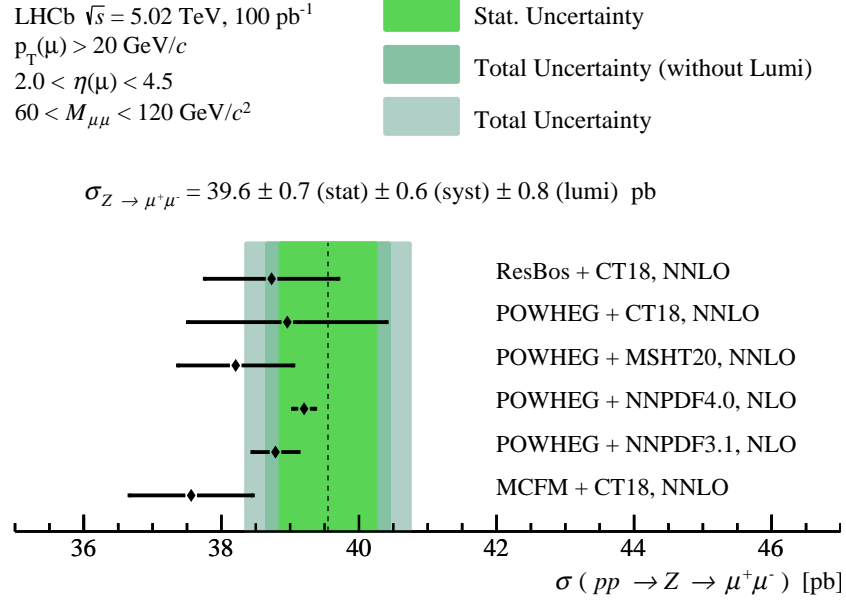


Figure 4: Comparison of the integrated cross-section, $\sigma_{Z \rightarrow \mu^+\mu^-}$, between data and theoretical predictions. The bands correspond to the data, with the inner band corresponding to the statistical uncertainty and the outer bands corresponding to the systematic uncertainty and total uncertainty.

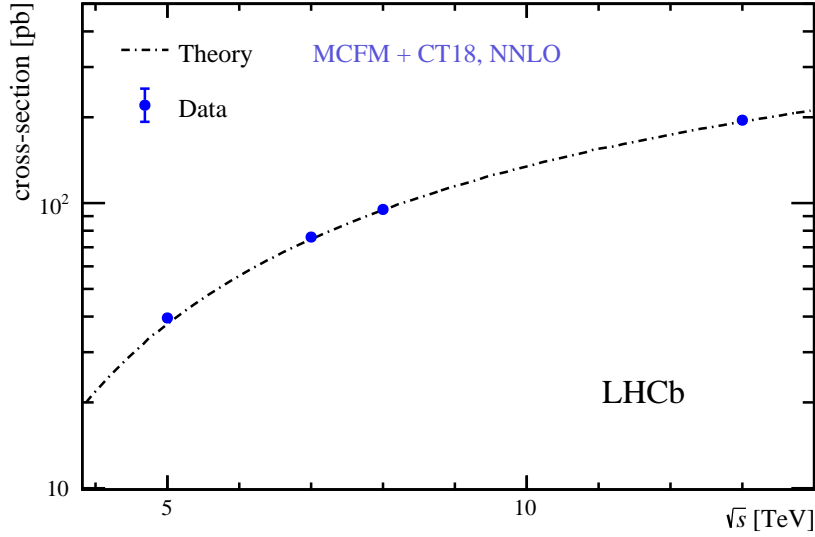


Figure 5: Measured $\sigma_{Z \rightarrow \mu^+\mu^-}$ for pp collisions, as a function of \sqrt{s} . The uncertainty on the data is too small to be visible. The data are overlaid with a curve showing the theoretical prediction.

6.4 Nuclear modification factors

The nuclear modification factors are determined based on the present measurements and those in Ref. [42]. Here, the statistical and systematic uncertainties (including uncertainties due to integrated luminosity) of the cross-sections measured between pp and $p\text{Pb}$ collisions are assumed to be fully uncorrelated when being propagated to the nuclear modification factors. Efficiency and background modeling uncertainties are also treated as fully uncorrelated, owing to the very different running conditions between pp and $p\text{Pb}$ collisions such as the heavier detector contamination from the much higher charged hadron multiplicities in case of $p\text{Pb}$. All other sources of systematic uncertainty are considered to be uncorrelated, an assumption that has negligible effect to the reported results.

The unique forward geometry coverage allows the LHCb detector to probe nPDFs at very small Bjorken- x ($10^{-4} < x < 10^{-3}$). The nuclear modification factors can be calculated using the pp cross-section measured here together with the Z boson production cross-section in $p\text{Pb}$ collisions measured in Ref. [42]. The nuclear modification factors are defined as the ratio of the cross-sections between $p\text{Pb}$ and pp collisions under the same muon rapidity acceptance. Due to the asymmetric beam energy in the $p\text{Pb}$ collision system, the muon rapidity acceptance ($2.0 < \eta < 4.5$) becomes $1.53 < y_\mu^* < 4.03$ in case of the forward collisions, and $-4.97 < y_\mu^* < -2.47$ in case of backward collisions, where y_μ^* represents the muon rapidity in the centre-of-mass frame. The two rapidity quantities are identical in pp collisions, $\eta_\mu \equiv y_\mu^*$, due to the symmetric beam energy. Forward collisions refer to the proton beam entering the LHCb detector along the positive direction of the z axis, while backward collisions correspond to the proton beam going in the opposite direction.

The cross-sections of the $p\text{Pb}$ collisions measured under different rapidity acceptances need to be corrected before being used to calculate the nuclear modification factors. The $k_{p\text{Pb}}$ factor corrects for the different η acceptance between $p\text{Pb}$ and pp collisions and can be calculated using POWHEG with the proton PDF set CTEQ6.1 [73],

$$k_{p\text{Pb}}^{\text{F}} = \frac{\sigma(pp, 2.0 < \eta < 4.5)}{\sigma(pp, 1.53 < \eta < 4.03)} = 0.706 \pm 0.002, \quad (6)$$

and

$$k_{p\text{Pb}}^{\text{B}} = \frac{\sigma(pp, 2.0 < \eta < 4.5)}{\sigma(pp, -4.97 < \eta < -2.47)} = 1.518 \pm 0.003, \quad (7)$$

for forward and backward collisions, respectively. The integrated nuclear modification factors can then be defined as follows

$$R_{p\text{Pb}}^{\text{F}} = k_{p\text{Pb}}^{\text{F}} \cdot \frac{\sigma(p\text{Pb}, 1.53 < y_\mu^* < 4.03)}{208 \cdot \sigma(pp, 2.0 < \eta < 4.5)}, \quad (8)$$

and

$$R_{p\text{Pb}}^{\text{B}} = k_{p\text{Pb}}^{\text{B}} \cdot \frac{\sigma(p\text{Pb}, -4.97 < y_\mu^* < -2.47)}{208 \cdot \sigma(pp, 2.0 < \eta < 4.5)}, \quad (9)$$

for forward and backwards $p\text{Pb}$ collisions, respectively, with 208 being the number of binary nucleon-nucleon collisions in $p\text{Pb}$ collisions.

The nuclear modification factors are calculated to be

$$R_{p\text{Pb}}^{\text{F}} = 1.2_{-0.3}^{+0.5} (\text{stat}) \pm 0.1 (\text{syst})$$

in the forward collisions, and

$$R_{pPb}^B = 3.6_{-0.9}^{+1.6} (\text{stat}) \pm 0.2 (\text{syst})$$

in the backward collisions. The large statistical uncertainties are due to the small size of the pPb data sample.

Based on the theoretical prediction of the cross-sections from Ref. [42] derived using FEWZ [74] at NNLO with EPS09 nPDFs [40] and MSTW08 PDF [41], the predicted R_{pPb} can be derived as $R_{pPb}^{\text{F, theo.}} = 0.906_{-0.007}^{+0.002}$ and $R_{pPb}^{\text{B, theo.}} = 0.929_{-0.028}^{+0.011}$ for the forward and backward collisions, respectively. The measurement and theoretical prediction agree within the uncertainties in the forward region, whereas there is some tension between the results in the backward region. However, due to the limited size of the pPb sample, the tension could be caused by a statistical fluctuation.

7 Conclusion

This paper reports the first measurement of Z boson production cross-section at the centre-of-mass energy $\sqrt{s} = 5.02$ TeV, using the LHCb 2017 pp collision dataset. The techniques employed in this analysis closely follow the techniques and strategies established in a previous LHCb Run 2 analysis [32]. The results show reasonable agreement with different Standard Model predictions. Combining with the first inclusive Z production result in pPb collisions at $\sqrt{s_{NN}} = 5.02$ TeV [42] the nuclear modification factors in the forward and backward regions have been measured for the first time.

Appendices

A Efficiency

Results of muon efficiencies used in the total Z -boson efficiency calculation are presented in Fig. 6 and Table 3.

B Final state radiation corrections

Tabulated results of final state radiation corrections used in the single differential cross-section measurements are presented in Tables 4 to 6.

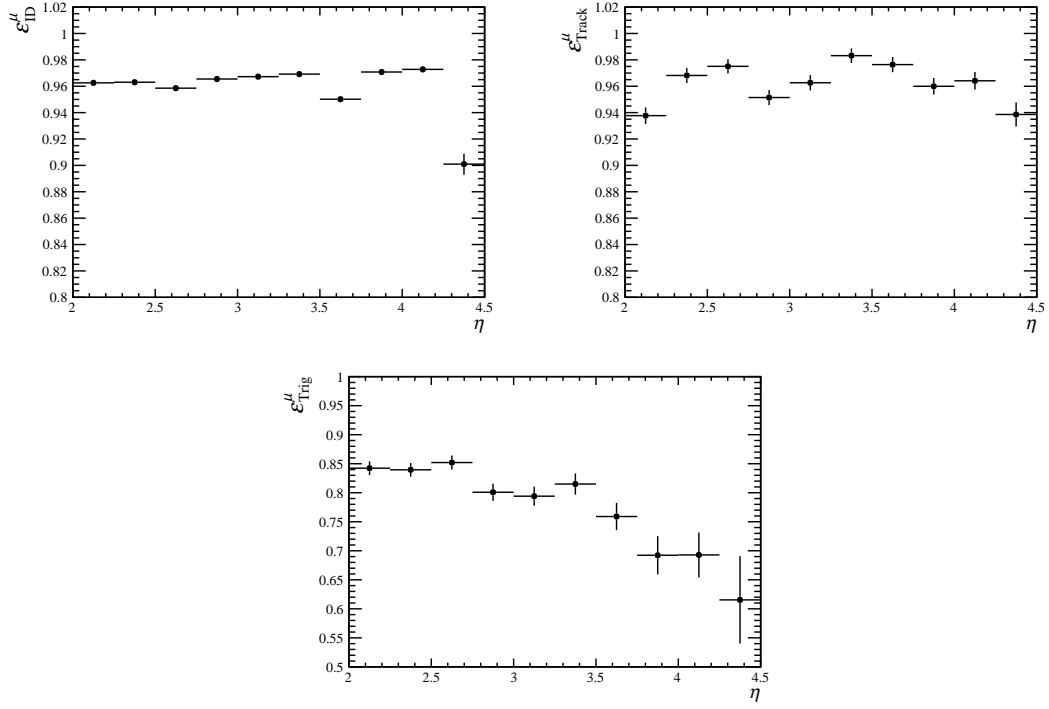


Figure 6: Muon tracking, identification and trigger efficiency as a function of pseudorapidity, estimated from the data and simulation at 5.02 TeV and 13 TeV.

Table 3: The muon tracking, muon identification and trigger efficiency in each pseudorapidity bin.

η	$\varepsilon_{\text{Track}}^{\mu} [\%]$	$\varepsilon_{\text{ID}}^{\mu} [\%]$	$\varepsilon_{\text{Trig}}^{\mu} [\%]$
[2.00, 2.25]	93.77	96.26	84.23
[2.25, 2.50]	96.82	96.30	83.95
[2.50, 2.75]	97.51	95.85	85.20
[2.75, 3.00]	95.14	96.55	80.08
[3.00, 3.25]	96.26	96.73	79.41
[3.25, 3.50]	98.32	96.92	81.50
[3.50, 3.75]	97.64	95.02	75.90
[3.75, 4.00]	96.00	97.08	69.23
[4.00, 4.25]	96.41	97.28	69.29
[4.25, 4.50]	93.86	90.10	61.54

Table 4: Final state radiation correction used in the y^Z cross-section measurement. The first uncertainty is statistical and the second is systematic.

y^Z	Correction
[2.000, 2.125]	1.018 \pm 0.004 \pm 0.092
[2.125, 2.250]	1.018 \pm 0.002 \pm 0.000
[2.250, 2.375]	1.019 \pm 0.002 \pm 0.006
[2.375, 2.500]	1.021 \pm 0.002 \pm 0.057
[2.500, 2.625]	1.021 \pm 0.001 \pm 0.046
[2.625, 2.750]	1.022 \pm 0.001 \pm 0.122
[2.750, 2.875]	1.024 \pm 0.002 \pm 0.009
[2.875, 3.000]	1.026 \pm 0.002 \pm 0.162
[3.000, 3.125]	1.026 \pm 0.002 \pm 0.070
[3.125, 3.250]	1.027 \pm 0.002 \pm 0.128
[3.250, 3.375]	1.027 \pm 0.002 \pm 0.011
[3.375, 3.625]	1.025 \pm 0.002 \pm 0.023
[3.625, 4.000]	1.020 \pm 0.004 \pm 0.001

Table 5: Final state radiation correction used in the p_T^Z cross-section measurement. The first uncertainty is statistical and the second is systematic.

p_T^Z [GeV/c]	Correction
[0.0, 2.2]	1.092 \pm 0.002 \pm 0.020
[2.2, 3.4]	1.080 \pm 0.002 \pm 0.018
[3.4, 4.6]	1.063 \pm 0.002 \pm 0.003
[4.6, 5.8]	1.044 \pm 0.002 \pm 0.015
[5.8, 7.2]	1.027 \pm 0.002 \pm 0.029
[7.2, 8.7]	1.012 \pm 0.002 \pm 0.025
[8.7, 10.5]	1.001 \pm 0.002 \pm 0.003
[10.5, 12.8]	0.987 \pm 0.002 \pm 0.006
[12.8, 15.4]	0.977 \pm 0.002 \pm 0.010
[15.4, 19.0]	0.968 \pm 0.002 \pm 0.005
[19.0, 34.0]	0.985 \pm 0.001 \pm 0.000
[34.0, 120.0]	1.038 \pm 0.002 \pm 0.000

Table 6: Final state radiation correction used in the ϕ_η^* cross-section measurement. The first uncertainty is statistical and the second is systematic.

ϕ_η^*	Correction
[0.00, 0.01]	1.035 \pm 0.002 \pm 3.802
[0.01, 0.02]	1.034 \pm 0.002 \pm 0.919
[0.02, 0.03]	1.032 \pm 0.002 \pm 1.384
[0.03, 0.05]	1.027 \pm 0.001 \pm 0.878
[0.05, 0.07]	1.021 \pm 0.002 \pm 1.060
[0.07, 0.10]	1.017 \pm 0.002 \pm 0.378
[0.10, 0.15]	1.013 \pm 0.002 \pm 0.220
[0.15, 0.20]	1.011 \pm 0.002 \pm 0.288
[0.20, 0.30]	1.010 \pm 0.002 \pm 0.236
[0.30, 0.60]	1.011 \pm 0.002 \pm 0.039
[0.60, 1.20]	1.017 \pm 0.006 \pm 0.001

C Correlation matrices

The calculated statistical correlation matrices are shown in Fig. 7 and presented in Tables 7 to 9. The correlation matrices for the efficiency uncertainty are shown in Fig. 8 for single differential cross-section measurements, and presented in Tables 10 to 12.

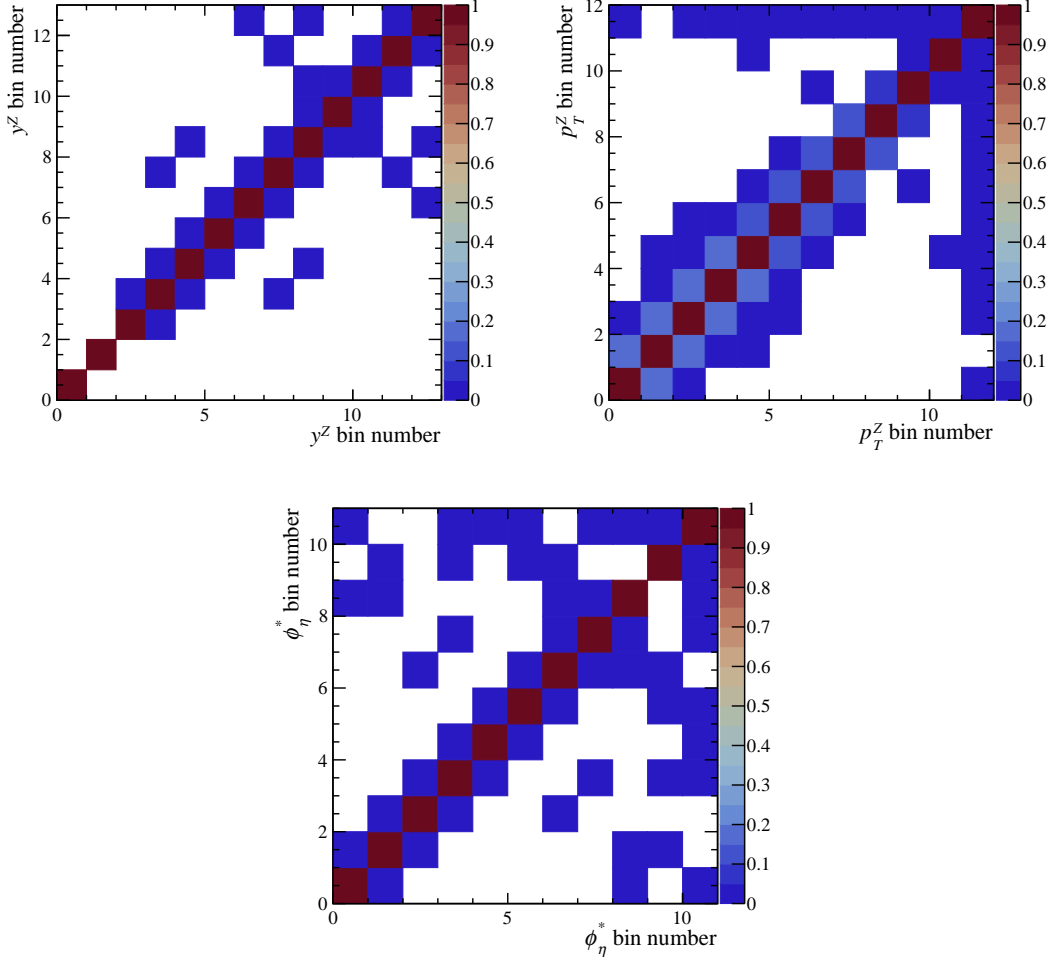


Figure 7: Statistical correlation matrices for the differential cross-section measurements as functions of (top-left) y^Z , (top-right) p_T^Z and (bottom) ϕ_η^* .

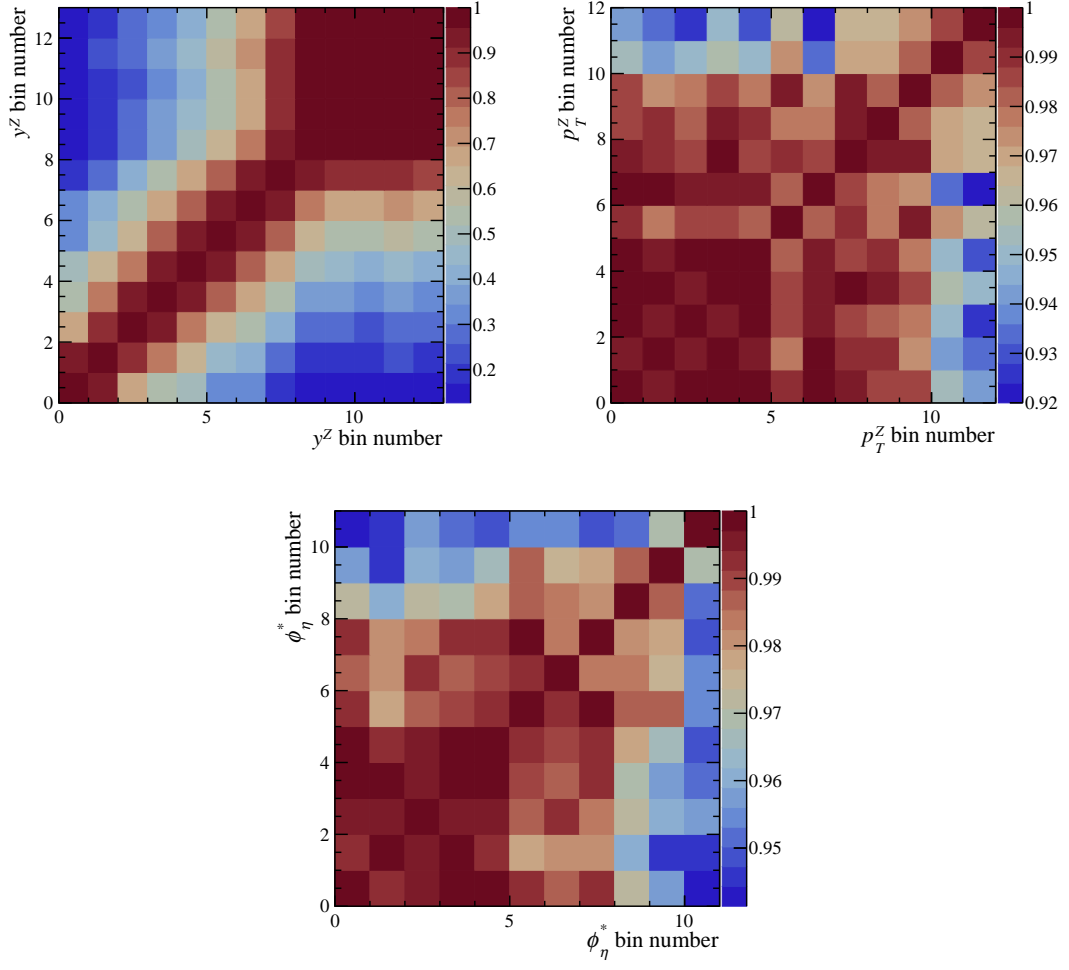


Figure 8: Correlation matrices for the efficiency uncertainties as functions of (top-left) y^Z , (top-right) p_T^Z and (bottom) ϕ_η^* .

Table 7: Statistical correlation matrix for the one-dimensional y^Z measurement.

Bin	1	2	3	4	5	6	7	8	9	10	11	12	13
1	1.00												
2	0.00	1.00											
3	0.00	0.00	1.00										
4	0.00	0.00	0.00	1.00									
5	0.00	0.00	0.00	0.01	1.00								
6	0.00	0.00	0.00	0.00	0.01	1.00							
7	0.00	0.00	0.00	0.00	0.00	0.01	1.00						
8	0.00	0.00	0.00	0.00	0.00	0.00	0.01	1.00					
9	0.00	0.00	0.00	0.00	0.00	0.00	0.00	0.01	1.00				
10	0.00	0.00	0.00	0.00	0.00	0.00	0.00	0.00	0.01	1.00			
11	0.00	0.00	0.00	0.00	0.00	0.00	0.00	0.00	0.00	0.01	1.00		
12	0.00	0.00	0.00	0.00	0.00	0.00	0.00	0.00	0.00	0.00	0.02	1.00	
13	0.00	0.00	0.00	0.00	0.00	0.00	0.00	0.00	0.00	0.00	0.00	0.00	1.00

Table 8: Statistical correlation matrix for the one-dimensional p_T^Z measurement.

Bin	1	2	3	4	5	6	7	8	9	10	11	12
1	1.00											
2	0.16	1.00										
3	0.00	0.18	1.00									
4	0.00	0.01	0.18	1.00								
5	0.00	0.00	0.01	0.18	1.00							
6	0.00	0.00	0.00	0.01	0.14	1.00						
7	0.00	0.00	0.00	0.00	0.01	0.12	1.00					
8	0.00	0.00	0.00	0.00	0.00	0.00	0.10	1.00				
9	0.00	0.00	0.00	0.00	0.00	0.00	0.00	0.10	1.00			
10	0.00	0.00	0.00	0.00	0.00	0.00	0.00	0.00	0.05	1.00		
11	0.00	0.00	0.00	0.00	0.00	0.00	0.00	0.00	0.00	0.04	1.00	
12	0.00	0.00	0.00	0.00	0.00	0.01	0.00	0.00	0.00	0.01	0.01	1.00

Table 9: Statistical correlation matrix for the one-dimensional ϕ_η^* measurement.

Bin	1	2	3	4	5	6	7	8	9	10	11
1	1.00										
2	0.01	1.00									
3	0.00	0.01	1.00								
4	0.00	0.00	0.01	1.00							
5	0.00	0.00	0.00	0.01	1.00						
6	0.00	0.00	0.00	0.00	0.00	1.00					
7	0.00	0.00	0.00	0.00	0.00	0.00	1.00				
8	0.00	0.00	0.00	0.00	0.00	0.00	0.00	1.00			
9	0.00	0.00	0.00	0.00	0.00	0.00	0.00	0.00	1.00		
10	0.00	0.00	0.00	0.00	0.00	0.00	0.00	0.00	0.00	1.00	
11	0.00	0.00	0.00	0.00	0.00	0.00	0.00	0.00	0.00	0.00	1.00

Table 10: Correlation matrix for the efficiency uncertainty of the one-dimensional y^Z measurement.

Bin	1	2	3	4	5	6	7	8	9	10	11	12	13
1	1.00												
2	0.92	1.00											
3	0.68	0.89	1.00										
4	0.56	0.74	0.93	1.00									
5	0.49	0.62	0.77	0.92	1.00								
6	0.34	0.47	0.65	0.81	0.95	1.00							
7	0.31	0.41	0.54	0.67	0.82	0.94	1.00						
8	0.19	0.28	0.40	0.53	0.69	0.81	0.93	1.00					
9	0.14	0.21	0.29	0.38	0.51	0.63	0.78	0.94	1.00				
10	0.13	0.19	0.27	0.35	0.44	0.54	0.69	0.87	0.99	1.00			
11	0.13	0.18	0.25	0.33	0.42	0.52	0.68	0.87	0.98	1.00	1.00		
12	0.16	0.22	0.29	0.37	0.46	0.57	0.72	0.89	0.99	1.00	1.00	1.00	
13	0.16	0.21	0.27	0.34	0.42	0.52	0.68	0.87	0.98	1.00	1.00	1.00	1.00

Table 11: Correlation matrix for the efficiency uncertainty of the one-dimensional p_T^Z measurement.

Bin	1	2	3	4	5	6	7	8	9	10	11	12
1	1.00											
2	1.00	1.00										
3	1.00	0.99	1.00									
4	1.00	1.00	1.00	1.00								
5	1.00	1.00	1.00	1.00	1.00							
6	0.99	0.98	0.99	0.99	0.98	1.00						
7	1.00	1.00	1.00	1.00	1.00	0.98	1.00					
8	0.99	0.99	0.99	1.00	0.99	0.99	0.99	1.00				
9	0.99	0.99	0.98	0.99	0.99	0.98	0.98	0.99	1.00			
10	0.98	0.98	0.98	0.99	0.98	0.99	0.97	0.99	0.98	1.00		
11	0.96	0.94	0.95	0.96	0.95	0.97	0.93	0.97	0.97	0.98	1.00	
12	0.94	0.93	0.93	0.95	0.93	0.96	0.92	0.97	0.97	0.98	0.99	1.00

Table 12: Correlation matrix for the efficiency uncertainty of the one-dimensional ϕ_η^* measurement.

Bin	1	2	3	4	5	6	7	8	9	10	11
1	1.00										
2	0.99	1.00									
3	0.99	1.00	1.00								
4	1.00	1.00	1.00	1.00							
5	1.00	0.99	0.99	1.00	1.00						
6	0.99	0.98	0.99	0.99	0.99	1.00					
7	0.99	0.98	0.99	0.99	0.99	0.99	1.00				
8	0.99	0.98	0.98	0.99	0.99	1.00	0.98	1.00			
9	0.97	0.96	0.97	0.97	0.98	0.99	0.98	0.98	1.00		
10	0.96	0.95	0.96	0.96	0.97	0.99	0.98	0.98	0.99	1.00	
11	0.94	0.95	0.96	0.95	0.95	0.96	0.95	0.95	0.95	0.97	1.00

D Summary of systematic uncertainties

The summarised systematic uncertainties for single differential cross-sections are shown in Tables 13 to 15.

Table 13: Systematic uncertainties on the single differential cross-sections in bins of y^Z , presented in percentage.

y^Z	Efficiency	Background	FSR	Closure
[2.000, 2.125]	1.42	0.04	2.10	0.45
[2.125, 2.250]	1.37	0.77	0.00	0.31
[2.250, 2.375]	1.32	0.62	0.02	0.34
[2.375, 2.500]	1.31	1.47	0.21	0.67
[2.500, 2.625]	1.32	1.42	0.13	1.17
[2.625, 2.750]	1.33	0.28	0.30	0.92
[2.750, 2.875]	1.36	0.52	0.02	0.89
[2.875, 3.000]	1.40	0.39	0.42	1.13
[3.000, 3.125]	1.46	0.51	0.23	0.68
[3.125, 3.250]	1.56	0.00	0.50	0.58
[3.250, 3.375]	1.63	0.00	0.07	1.01
[3.375, 3.625]	1.85	1.14	0.34	0.85
[3.625, 4.000]	2.23	0.00	0.21	0.80

Table 14: Systematic uncertainties on the single differential cross-sections in bins of p_T^Z , presented in percentage.

p_T^Z [GeV/c]	Efficiency	Background	FSR	Closure	Calibration	Unfolding
[0.0, 2.2]	1.42	0.56	1.15	0.43	0.13	0.54
[2.2, 3.4]	1.41	0.50	0.64	0.37	0.40	1.73
[3.4, 4.6]	1.43	0.09	0.09	0.50	0.28	1.66
[4.6, 5.8]	1.40	0.04	0.55	0.05	0.74	1.18
[5.8, 7.2]	1.43	0.25	1.27	0.12	0.91	0.36
[7.2, 8.7]	1.38	0.60	1.19	2.11	0.59	0.02
[8.7, 10.5]	1.44	0.20	0.14	0.50	0.54	0.04
[10.5, 12.8]	1.39	1.34	0.48	0.97	0.31	0.03
[12.8, 15.4]	1.39	2.00	1.11	0.18	0.36	0.01
[15.4, 19.0]	1.39	1.10	0.71	1.16	0.17	0.00
[19.0, 34.0]	1.37	1.09	0.09	1.97	0.10	0.00
[34.0, 120.0]	1.36	1.03	0.31	2.18	0.16	0.00

Table 15: Systematic uncertainties on the single differential cross-sections in bins of ϕ_η^* , presented in percentage.

ϕ_η^*	Efficiency	Background	FSR	Closure
[0.00, 0.01]	1.41	1.10	0.81	0.01
[0.01, 0.02]	1.42	0.43	0.21	0.00
[0.02, 0.03]	1.41	0.14	0.36	0.12
[0.03, 0.05]	1.42	0.52	0.28	0.45
[0.05, 0.07]	1.41	0.01	0.50	0.44
[0.07, 0.10]	1.39	0.29	0.24	2.22
[0.10, 0.15]	1.39	1.45	0.25	0.81
[0.15, 0.20]	1.39	0.82	0.63	1.35
[0.20, 0.30]	1.38	0.77	0.97	1.00
[0.30, 0.60]	1.37	1.45	0.61	2.72
[0.60, 1.20]	1.38	0.09	0.13	2.13

E Numerical results of single differential cross-sections

The measured single differential cross-sections in bins of y^Z , p_T^Z and ϕ_η^* are presented in Tables 16 to 18.

Table 16: Measured single differential cross-sections in bins of y^Z . The first uncertainty is statistical, the second systematic, and the third is from the uncertainty on the integrated luminosity.

y^Z	$d\sigma(Z \rightarrow \mu^+ \mu^-)/dy^Z$ [pb]						
[2.000, 2.125]	4.4	±	0.7	±	0.1	±	0.1
[2.125, 2.250]	14.6	±	1.2	±	0.2	±	0.3
[2.250, 2.375]	24.3	±	1.5	±	0.4	±	0.5
[2.375, 2.500]	27.5	±	1.6	±	0.6	±	0.6
[2.500, 2.625]	36.1	±	1.8	±	0.8	±	0.7
[2.625, 2.750]	39.9	±	2.0	±	0.7	±	0.8
[2.750, 2.875]	42.6	±	2.0	±	0.7	±	0.9
[2.875, 3.000]	38.8	±	1.9	±	0.7	±	0.8
[3.000, 3.125]	30.8	±	1.7	±	0.5	±	0.6
[3.125, 3.250]	25.5	±	1.6	±	0.4	±	0.5
[3.250, 3.375]	16.0	±	1.3	±	0.3	±	0.3
[3.375, 3.625]	6.8	±	0.6	±	0.2	±	0.1
[3.625, 4.000]	0.7	±	0.2	±	0.0	±	0.0

Table 17: Measured single differential cross-sections in bins of p_{T}^Z . The first uncertainty is statistical, the second systematic, and the third is due to the luminosity.

p_{T}^Z [GeV/c]	$d\sigma(Z \rightarrow \mu^+\mu^-)/dp_{\text{T}}^Z$ [pb/(GeV/c)]						
[0.0, 2.2]	1.769	±	0.105	±	0.036	±	0.035
[2.2, 3.4]	2.77	±	0.17	±	0.07	±	0.06
[3.4, 4.6]	3.23	±	0.19	±	0.07	±	0.06
[4.6, 5.8]	2.71	±	0.17	±	0.06	±	0.05
[5.8, 7.2]	2.27	±	0.14	±	0.05	±	0.05
[7.2, 8.7]	2.09	±	0.13	±	0.06	±	0.04
[8.7, 10.5]	1.806	±	0.110	±	0.030	±	0.036
[10.5, 12.8]	1.234	±	0.076	±	0.028	±	0.025
[12.8, 15.4]	0.911	±	0.063	±	0.025	±	0.018
[15.4, 19.0]	0.759	±	0.050	±	0.017	±	0.015
[19.0, 34.0]	0.328	±	0.016	±	0.009	±	0.007
[34.0, 120.0]	0.0325	±	0.0021	±	0.0009	±	0.0007

Table 18: Measured single differential cross-sections in bins of ϕ_{η}^* . The first uncertainty is statistical, the second systematic, and the third is due to the luminosity.

ϕ_{η}^*	$d\sigma(Z \rightarrow \mu^+\mu^-)/d\phi_{\eta}^*$ [pb]						
[0.00, 0.01]	468.5	±	23.8	±	9.2	±	9.4
[0.01, 0.02]	442.4	±	23.4	±	6.6	±	8.8
[0.02, 0.03]	384.6	±	21.9	±	5.6	±	7.7
[0.03, 0.05]	311.6	±	13.8	±	5.0	±	6.2
[0.05, 0.07]	212.1	±	11.5	±	3.3	±	4.2
[0.07, 0.10]	160.4	±	8.0	±	4.2	±	3.2
[0.10, 0.15]	87.63	±	4.51	±	1.91	±	1.75
[0.15, 0.20]	45.59	±	3.31	±	1.00	±	0.91
[0.20, 0.30]	24.21	±	1.70	±	0.51	±	0.48
[0.30, 0.60]	6.30	±	0.49	±	0.22	±	0.13
[0.60, 1.20]	0.571	±	0.108	±	0.015	±	0.011

References

- [1] P. J. Rijken and W. L. van Neerven, *Order α_s^2 contributions to the Drell-Yan cross-section at fixed target energies*, Phys. Rev. **D51** (1995) 44, [arXiv:hep-ph/9408366](#).
- [2] R. Hamberg, W. L. van Neerven, and T. Matsuura, *A complete calculation of the order α_s^2 correction to the Drell-Yan K factor*, Nucl. Phys. **B359** (1991) 343, [Erratum: Nucl. Phys. **B644**, 403–404 (2002)].
- [3] R. V. Harlander and W. B. Kilgore, *Next-to-next-to-leading order Higgs production at hadron colliders*, Phys. Rev. Lett. **88** (2002) 201801, [arXiv:hep-ph/0201206](#).
- [4] W. L. van Neerven and E. B. Zijlstra, *The $O(\alpha_s^2)$ corrected Drell-Yan K factor in the DIS and \overline{MS} scheme*, Nucl. Phys. **B382** (1992) 11, [Erratum: Nucl. Phys. **B680**, 513–514 (2004)].
- [5] C. Anastasiou, L. J. Dixon, K. Melnikov, and F. Petriello, *High precision QCD at hadron colliders: Electroweak gauge boson rapidity distributions at NNLO*, Phys. Rev. **D69** (2004) 094008, [arXiv:hep-ph/0312266](#).
- [6] I. Scimemi and A. Vladimirov, *Non-perturbative structure of semi-inclusive deep-inelastic and Drell-Yan scattering at small transverse momentum*, JHEP **06** (2020) 137, [arXiv:1912.06532](#).
- [7] M. Bury *et al.*, *PDF bias and flavor dependence in TMD distributions*, JHEP **10** (2022) 118, [arXiv:2201.07114](#).
- [8] S. Camarda, L. Cieri, and G. Ferrera, *Drell-Yan lepton-pair production: qT resummation at N^3LL accuracy and fiducial cross sections at N^3LO* , Phys. Rev. **D104** (2021) L111503, [arXiv:2103.04974](#).
- [9] C. Duhr and B. Mistlberger, *Lepton-pair production at hadron colliders at N^3LO in QCD*, JHEP **03** (2022) 116, [arXiv:2111.10379](#).
- [10] H1, ZEUS Collaboration, F. D. Aaron *et al.*, *Combined measurement and QCD analysis of the inclusive e^+p scattering cross sections at HERA*, JHEP **01** (2010) 109, [arXiv:0911.0884](#).
- [11] H1, ZEUS Collaboration, H. Abramowicz *et al.*, *Combination of measurements of inclusive deep inelastic $e^\pm p$ scattering cross sections and QCD analysis of HERA data*, Eur. Phys. J. **C75** (2015) 580, [arXiv:1506.06042](#).
- [12] CDF collaboration, F. Abe *et al.*, *Forward-backward charge asymmetry of electron pairs above the Z^0 pole*, Phys. Rev. Lett. **77** (1996) 2616.
- [13] CDF collaboration, D. Acosta *et al.*, *Measurement of the forward-backward charge asymmetry from $W \rightarrow e\nu$ production in $p\bar{p}$ collisions at $\sqrt{s} = 1.96$ TeV*, Phys. Rev. **D71** (2005) 051104, [arXiv:hep-ex/0501023](#).
- [14] CDF collaboration, T. A. Aaltonen *et al.*, *Measurement of $d\sigma/dy$ of Drell-Yan e^+e^- pairs in the Z Mass Region from $p\bar{p}$ Collisions at $\sqrt{s} = 1.96$ TeV*, Phys. Lett. **B692** (2010) 232, [arXiv:0908.3914](#).

- [15] CDF collaboration, T. Aaltonen *et al.*, *Measurement of the inclusive jet cross section at the Fermilab Tevatron $p\bar{p}$ collider using a cone-based jet algorithm*, Phys. Rev. **D78** (2008) 052006, [arXiv:0807.2204](#), [Erratum: Phys. Rev. **D79**, 119902 (2009)].
- [16] D0 collaboration, V. M. Abazov *et al.*, *Measurement of the muon charge asymmetry from W boson decays*, Phys. Rev. **D77** (2008) 011106, [arXiv:0709.4254](#).
- [17] D0 collaboration, V. M. Abazov *et al.*, *Measurement of the ratios of the $Z/\gamma^* + \geq n$ jet production cross sections to the total inclusive Z/γ^* cross section in $p\bar{p}$ collisions at $\sqrt{s} = 1.96$ TeV*, Phys. Lett. **B658** (2008) 112, [arXiv:hep-ex/0608052](#).
- [18] D0 collaboration, V. M. Abazov *et al.*, *Measurement of the electron charge asymmetry in $p\bar{p} \rightarrow W + X \rightarrow e\nu + X$ decays in $p\bar{p}$ collisions at $\sqrt{s} = 1.96$ TeV*, Phys. Rev. **D91** (2015) 032007, [arXiv:1412.2862](#), [Erratum: Phys. Rev. **D91**, 079901 (2015)].
- [19] D0 collaboration, V. M. Abazov *et al.*, *Measurement of the inclusive jet cross-section in $p\bar{p}$ collisions at $\sqrt{s} = 1.96$ TeV*, Phys. Rev. Lett. **101** (2008) 062001, [arXiv:0802.2400](#).
- [20] ATLAS collaboration, G. Aad *et al.*, *Measurement of the inclusive W^\pm and Z/γ^* cross sections in the electron and muon decay channels in pp collisions at $\sqrt{s} = 7$ TeV with the ATLAS detector*, Phys. Rev. **D85** (2012) 072004, [arXiv:1109.5141](#).
- [21] ATLAS collaboration, G. Aad *et al.*, *Measurement of the transverse momentum and ϕ_η^* distributions of Drell–Yan lepton pairs in proton–proton collisions at $\sqrt{s} = 8$ TeV with the ATLAS detector*, Eur. Phys. J. **C76** (2016) 291, [arXiv:1512.02192](#).
- [22] CMS collaboration, S. Chatrchyan *et al.*, *Measurement of the muon charge asymmetry in inclusive $pp \rightarrow W + X$ production at $\sqrt{s} = 7$ TeV and an improved determination of light parton distribution functions*, Phys. Rev. **D90** (2014) 032004, [arXiv:1312.6283](#).
- [23] CMS collaboration, S. Chatrchyan *et al.*, *Measurement of the electron charge asymmetry in inclusive W production in pp collisions at $\sqrt{s} = 7$ TeV*, Phys. Rev. Lett. **109** (2012) 111806, [arXiv:1206.2598](#).
- [24] ATLAS collaboration, G. Aad *et al.*, *Measurement of the transverse momentum distribution of Drell–Yan lepton pairs in proton–proton collisions at $\sqrt{s} = 13$ TeV with the ATLAS detector*, Eur. Phys. J. **C80** (2020) 616, [arXiv:1912.02844](#).
- [25] CMS collaboration, A. M. Sirunyan *et al.*, *Measurements of differential Z boson production cross sections in proton–proton collisions at $\sqrt{s} = 13$ TeV*, JHEP **12** (2019) 061, [arXiv:1909.04133](#).
- [26] LHCb collaboration, R. Aaij *et al.*, *Measurement of the forward W boson production cross-section in pp collisions at $\sqrt{s} = 7$ TeV*, JHEP **12** (2014) 079, [arXiv:1408.4354](#).
- [27] LHCb collaboration, R. Aaij *et al.*, *Measurement of the forward Z boson cross-section in pp collisions at $\sqrt{s} = 7$ TeV*, JHEP **08** (2015) 039, [arXiv:1505.07024](#).
- [28] LHCb collaboration, R. Aaij *et al.*, *Measurement of $Z \rightarrow e^+e^-$ production at $\sqrt{s} = 8$ TeV*, JHEP **05** (2015) 109, [arXiv:1503.00963](#).

- [29] LHCb collaboration, R. Aaij *et al.*, *Measurement of forward W and Z boson production in pp collisions at $\sqrt{s}=8$ TeV*, JHEP **01** (2016) 155, [arXiv:1511.08039](#).
- [30] LHCb collaboration, R. Aaij *et al.*, *Measurement of forward $W \rightarrow e\nu$ production in pp collisions at $\sqrt{s}=8$ TeV*, JHEP **10** (2016) 030, [arXiv:1608.01484](#).
- [31] LHCb collaboration, R. Aaij *et al.*, *Measurement of the forward Z boson production cross-section in pp collisions at $\sqrt{s}=13$ TeV*, JHEP **09** (2016) 136, [arXiv:1607.06495](#).
- [32] LHCb collaboration, R. Aaij *et al.*, *Precision measurement of forward Z boson production in proton-proton collisions at $\sqrt{s}=13$ TeV*, JHEP **07** (2022) 026, [arXiv:2112.07458](#).
- [33] S. Dulat *et al.*, *New parton distribution functions from a global analysis of quantum chromodynamics*, Phys. Rev. **D93** (2016) 033006, [arXiv:1506.07443](#).
- [34] L. A. Harland-Lang, A. D. Martin, P. Motylinski, and R. S. Thorne, *Parton distributions in the LHC era: MMHT 2014 PDFs*, Eur. Phys. J. **C75** (2015) 204, [arXiv:1412.3989](#).
- [35] NNPDF collaboration, R. D. Ball *et al.*, *Parton distributions for the LHC Run II*, JHEP **04** (2015) 040, [arXiv:1410.8849](#).
- [36] T.-J. Hou *et al.*, *New CTEQ global analysis of quantum chromodynamics with high-precision data from the LHC*, Phys. Rev. **D103** (2021) 014013, [arXiv:1912.10053](#).
- [37] NNPDF collaboration, R. D. Ball *et al.*, *Parton distributions from high-precision collider data*, Eur. Phys. J. **C77** (2017) 663, [arXiv:1706.00428](#).
- [38] NNPDF collaboration, R. D. Ball *et al.*, *The path to proton structure at 1% accuracy*, Eur. Phys. J. **C82** (2022) 428, [arXiv:2109.02653](#).
- [39] S. Bailey *et al.*, *Parton distributions from LHC, HERA, Tevatron and fixed target data: MSHT20 PDFs*, Eur. Phys. J. **C81** (2021) 341, [arXiv:2012.04684](#).
- [40] K. J. Eskola, H. Paukkunen, and C. A. Salgado, *EPS09: A new generation of NLO and LO nuclear parton distribution functions*, JHEP **04** (2009) 065, [arXiv:0902.4154](#).
- [41] A. D. Martin, W. J. Stirling, R. S. Thorne, and G. Watt, *Parton distributions for the LHC*, Eur. Phys. J. **C63** (2009) 189, [arXiv:0901.0002](#).
- [42] LHCb collaboration, R. Aaij *et al.*, *Observation of Z production in proton-lead collisions at LHCb*, JHEP **09** (2014) 030, [arXiv:1406.2885](#).
- [43] LHCb collaboration, R. Aaij *et al.*, *Precision luminosity measurements at LHCb*, JINST **9** (2014) P12005, [arXiv:1410.0149](#).
- [44] A. Banfi *et al.*, *Optimisation of variables for studying dilepton transverse momentum distributions at hadron colliders*, Eur. Phys. J. **C71** (2011) 1600, [arXiv:1009.1580](#).
- [45] LHCb collaboration, A. A. Alves Jr. *et al.*, *The LHCb detector at the LHC*, JINST **3** (2008) S08005.

- [46] LHCb collaboration, R. Aaij *et al.*, *LHCb detector performance*, Int. J. Mod. Phys. **A30** (2015) 1530022, [arXiv:1412.6352](#).
- [47] R. Aaij *et al.*, *Performance of the LHCb Vertex Locator*, JINST **9** (2014) P09007, [arXiv:1405.7808](#).
- [48] LHCb collaboration, *LHCb reoptimized detector design and performance: Technical Design Report*, CERN-LHCC-2003-030, 2003.
- [49] P. d’Argent *et al.*, *Improved performance of the LHCb Outer Tracker in LHC Run 2*, JINST **12** (2017) P11016, [arXiv:1708.00819](#).
- [50] A. A. Alves Jr. *et al.*, *Performance of the LHCb muon system*, JINST **8** (2013) P02022, [arXiv:1211.1346](#).
- [51] R. Aaij *et al.*, *The LHCb trigger and its performance in 2011*, JINST **8** (2013) P04022, [arXiv:1211.3055](#).
- [52] T. Sjöstrand, S. Mrenna, and P. Skands, *PYTHIA 6.4 physics and manual*, JHEP **05** (2006) 026, [arXiv:hep-ph/0603175](#).
- [53] C. Bierlich *et al.*, *A comprehensive guide to the physics and usage of PYTHIA 8.3*, doi: 10.21468/SciPostPhysCodeb.8 [arXiv:2203.11601](#).
- [54] I. Belyaev *et al.*, *Handling of the generation of primary events in Gauss, the LHCb simulation framework*, J. Phys. Conf. Ser. **331** (2011) 032047.
- [55] N. Davidson, T. Przedzinski, and Z. Was, *PHOTOS interface in C++: Technical and physics documentation*, Comp. Phys. Comm. **199** (2016) 86, [arXiv:1011.0937](#).
- [56] Geant4 collaboration, J. Allison *et al.*, *Geant4 developments and applications*, IEEE Trans. Nucl. Sci. **53** (2006) 270.
- [57] M. Clemencic *et al.*, *The LHCb simulation application, Gauss: Design, evolution and experience*, J. Phys. Conf. Ser. **331** (2011) 032023.
- [58] J. Campbell and T. Neumann, *Precision Phenomenology with MCFM*, JHEP **12** (2019) 034, [arXiv:1909.09117](#).
- [59] LHCb collaboration, R. Aaij *et al.*, *Measurement of the W boson mass*, JHEP **01** (2022) 036, [arXiv:2109.01113](#).
- [60] LHCb collaboration, R. Aaij *et al.*, *Measurement of the track reconstruction efficiency at LHCb*, JINST **10** (2015) P02007, [arXiv:1408.1251](#).
- [61] H. B. Prosper and L. Lyons, eds., *Proceedings, PHYSTAT 2011 Workshop on Statistical Issues Related to Discovery Claims in Search Experiments and Unfolding, CERN, Geneva, Switzerland 17-20 January 2011*, CERN Yellow Reports: Conference Proceedings, (Geneva), CERN, 2011. doi: 10.5170/CERN-2011-006.
- [62] G. D’Agostini, *A multidimensional unfolding method based on Bayes’ theorem*, Nucl. Instrum. Meth. **A362** (1995) 487.

- [63] C. Balazs and C. P. Yuan, *Soft gluon effects on lepton pairs at hadron colliders*, Phys. Rev. **D56** (1997) 5558, [arXiv:hep-ph/9704258](#).
- [64] T. Adye, *Unfolding algorithms and tests using RooUnfold*, CERN-2011-006 (2011) 313, [arXiv:1105.1160](#).
- [65] J. C. Collins, D. E. Soper, and G. F. Sterman, *Transverse momentum distribution in Drell-Yan pair and W and Z boson production*, Nucl. Phys. **B250** (1985) 199.
- [66] J. C. Collins and D. E. Soper, *Back-to-back jets in QCD*, Nucl. Phys. **B193** (1981) 381, [Erratum: Nucl. Phys. B **213**, 545 (1983)].
- [67] J. C. Collins and D. E. Soper, *Back-to-back jets: fourier transform from B to K-transverse*, Nucl. Phys. **B197** (1982) 446.
- [68] P. Nason, *A New method for combining NLO QCD with shower Monte Carlo algorithms*, JHEP **11** (2004) 040, [arXiv:hep-ph/0409146](#).
- [69] S. Frixione, P. Nason, and C. Oleari, *Matching NLO QCD computations with Parton Shower simulations: the POWHEG method*, JHEP **11** (2007) 070, [arXiv:0709.2092](#).
- [70] S. Alioli, P. Nason, C. Oleari, and E. Re, *NLO vector-boson production matched with shower in POWHEG*, JHEP **07** (2008) 060, [arXiv:0805.4802](#).
- [71] S. Alioli, P. Nason, C. Oleari, and E. Re, *A general framework for implementing NLO calculations in shower Monte Carlo programs: the POWHEG BOX*, JHEP **06** (2010) 043, [arXiv:1002.2581](#).
- [72] T. Sjöstrand, S. Mrenna, and P. Skands, *A brief introduction to PYTHIA 8.1*, Comput. Phys. Commun. **178** (2008) 852, [arXiv:0710.3820](#).
- [73] J. Pumplin *et al.*, *New generation of parton distributions with uncertainties from global QCD analysis*, JHEP **07** (2002) 012, [arXiv:hep-ph/0201195](#).
- [74] Y. Li and F. Petriello, *Combining QCD and electroweak corrections to dilepton production in FEWZ*, Phys. Rev. **D86** (2012) 094034, [arXiv:1208.5967](#).